Review article

Graphitic Carbon Nitride (g-C_3N_4) and its Derivatives as Catalysts for Hydrogen Production.

Noof A.Alrekayan [a] ,Amirah S.Almajnuni[a], Alanoud M.Alsarheed, Laila S Alqarni[a1]

[a] Department of Chemistry, College of Science, Imam Mohammad Ibn Saud Islamic University (IMSIU), Riyadh 11623, Saudi Arabia

Abstract **This review aims to offer a comprehensive and critical overview of graphitic carbon nitride (g-C_3N_4) and its unique derivatives as strategic catalysts for the production of sustainable hydrogen. We systematically examine the relationship between various synthetic pathways, such as thermal condensation, chemical vapor deposition, hydrothermal processing, and template configurations, and their direct effects on the final morphological and catalytic properties, going beyond simple material descriptions. The primary goal of this paper is to assess recent significant advancements in efficiency-enhancement techniques, with particular emphasis on heteroatom doping, sophisticated 2D/2D heterojunction frameworks, Z-scheme/S-scheme designs, defect engineering, and the combination of bimetallic and single-atom co-catalysts. The mechanisms underlying charge-carrier dynamics, active-site distribution, and light-driven redox pathways are fully explained. Finally, this review addresses lingering technical bottlenecks such as rapid charge recombination and scalability, concluding with actionable future perspectives and techno-economic insights necessary to transition g-C_3N_4 architectures from bench-scale research to industrial-level green hydrogen production.**

Keywords:g-C_3N_4; Graphitic Carbon Nitride; Hydrogen Production; Photocatalysis.

Address for correspondence: Department of Chemistry, College of Science, Imam Mohammad Ibn Saud Islamic University (IMSIU), Riyadh 11623, Saudi Arabia
Email: Lassalqarni@imamu.edu.sa
Received: 15.05.2026; **Revision:** 28.05.2026; **Accepted:** 01.07.2026; **Published:** 30.07.2026

1. INTRODUCTION

In response to global energy shortages and environmental degradation, semiconductor-based photocatalysis has emerged as a promising green technology that utilizes solar energy to drive photocatalytic redox reactions. While traditional inorganic semiconductors (ISCs) like TiO_2, SnO_2, and ZnO offer high carrier mobility and excellent stability [1], their practical applications are often limited. For instance, anatase TiO_2, the historical standard in photocatalysis, possesses a wide bandgap (3.0–3.2 eV), restricting its activation to the ultraviolet (UV) region, which constitutes only 3% to 4% of the solar spectrum [2]. Although various modification strategies (such as doping, nanostructuring, and co-catalyst loading) have been employed to shift its response into the visible light spectrum [3], the need for inherently visible-light-active materials remains critical. The metal-free polymeric graphitic carbon nitride (g-C_3N_4) has attracted considerable attention in photocatalysis in recent years due to its distinct electrical band structure, affordability, and easy synthesis. A narrow bandgap of 2.7 eV allows g-C_3N_4 to be excited by visible light, making it superior to standard TiO_2. Consequently, g-C_3N_4 holds great potential in diverse photocatalytic applications, including pollutant degradation, sterilization, hydrogen production, and CO_2 reduction. It has

also shown encouraging results in emerging areas such as tumor treatment [4] and H_2O_2 generation [5].

However, pristine g-C_3N_4 suffers from several limitations, such as a low specific surface area, a narrow visible light absorption threshold (~450 nm), and rapid recombination of photogenerated electron-hole pairs [6-8].

To advance green hydrogen generation, it is especially important to overcome these barriers. Currently, most hydrogen produced worldwide is derived from hydrocarbons as "grey hydrogen," which causes significant CO_2 emissions [9]. While solar-powered water electrolysis provides a zero-emission alternative, it accounts for only 5% of global green hydrogen production [10, 11]. Recent studies have focused on chemical and structural modifications of g-C_3N_4 to close this efficiency gap. Techniques such as molecular doping, including sulfur doping to reduce the bandgap to 2.63 eV, morphology control, and co-catalyst incorporation have produced encouraging outcomes. Earth-abundant bimetallic co-catalysts such as CoNi or NiS, as well as precious metals such as Pt (3 wt%), have been shown to significantly accelerate electron transfer dynamics [12, 13]. For instance, combining CoNi with g-C_3N_4 reduced charge recombination and increased hydrogen evolution efficiency by 188-fold, reaching 354.4 μmol h^{-1} g^{-1} [14, 15].

In this review, we comprehensively focus on (g-C_3N_4) as a catalyst for hydrogen generation. The discussion begins with the inherent limitations of conventional inorganic photocatalysts and the rationale behind the shift toward organic semiconductors. Drawing on the unique structural characteristics, electronic properties, and photocatalytic mechanisms of g-C_3N_4, we systematically examine the diverse strategies developed to enhance its catalytic performance. Furthermore, we provide a critical assessment of the role of g-C_3N_4 in promoting sustainable hydrogen production, highlighting recent progress, persisting challenges, and potential future research directions.

2. Synthesis Methods of Graphitic Carbon Nitride (g-C_3N_4)

Melamine, melam, and melon are molecular compounds based on heptazine and triazine structures, with the coplanar tri-s-triazine unit serving as the fundamental unit of the g-C_3N_4 framework. As shown in **Figure 1**, triazine (C_3N_3) and tri-s-triazine/heptazine (C_6N_7) rings represent the primary structural units of g-C_3N_4 [16].

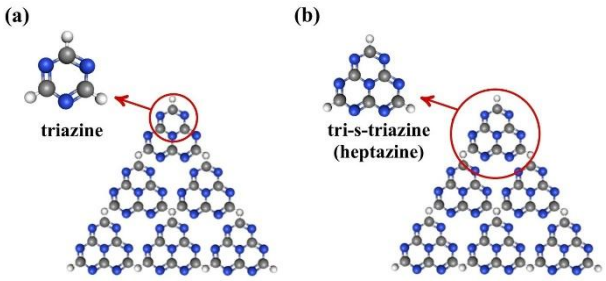

Figure 1. Structural configurations of g-C_3N_4 frameworks illustrating (a) the triazine (C_3N_3) and
(b) the tri-s-triazine/heptazine (C_6N_7) recurring units, showcasing the fundamental coordination
boundaries that dictate crystalline stability and chemical inertness during catalytic exposure.

This architectural variation is crucial; under operating conditions, the heptazine-based framework shows higher chemical and thermodynamic stability than the triazine form. A structural blueprint for visible-light activation is established by the distribution of localized electron density within these localized rings, which directly determines the principal coordinates for ensuing chemical changes, defect engineering, and co-catalyst anchoring [16].

The synthesis of graphitic carbon nitride (g-C_3N_4) has seen remarkable advancements over the years, providing researchers with a diverse set of strategies to fine-tune its properties for specific photocatalytic applications. As illustrated in **Figure 2**, these advancements are reflected in the various synthesis methods, each offering unique advantages and limitations. g-C_3N_4 can be synthesized through the thermal condensation of various precursors, containing cyanamide [17], dicyanamide [18], melamine [19], urea [20], and thiourea [21].

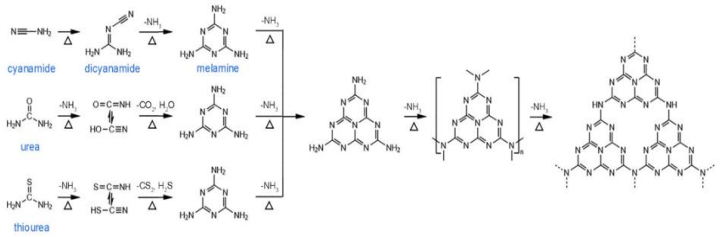

Figure 2. Synthetic reaction pathways for the thermal condensation of nitrogen-rich precursors
(cyanamide, dicyanamide, melamine, urea, and thiourea) into the extended g-C3N4 polymeric
matrix, highlighting the consecutive deamination stages required for full polymerization [22], Copyright © 2021 MDPI

As illustrated in Figures 2 and 3, the selection of the initial chemical precursor directly governs
the final polymerization degree, texturing, and native defect density of the resulting g-C_3N_4. For instance, oxygen-containing precursors like urea undergo self-sacrificial gas evolution during
calcination, resulting in a highly porous structure with an elevated specific surface area
compared to the more dense, bulk configurations produced by pristine melamine.
Understanding these phase boundaries allows researchers to deliberately tailor the initial
surface properties of the catalyst framework [19, 20].

2.1 Thermal polymerization

Thermal polymerization of inexpensive precursors such as melamine, urea, cyanamide, dicyanamide, thiourea, and cyanuric acid represents one of the most extensively used methods for synthesizing g-C_3N_4. This technique typically

involves heating the precursors at moderate temperatures (500-600 °C) under an inert gas atmosphere, as illustrated in **Figure 3**. Through this process, a layered g-C_3N_4 structure with a relatively high surface area is produced, making the material highly effective for various photocatalytic applications. The simplicity and cost-efficiency of this method have significantly contributed to its widespread adoption [23-25].

Figure 3. The multilayer g-C_3N_4 network is formed via the sequential deamination stages through cyanourea, melam, and melon intermediates in the detailed chemical steps of the thermal condensation of the melamine precursor.

The structural transformation shown in Figure 3 highlights the thermodynamic temperature windows required to achieve complete polymerization. Monitoring these chemical phases is essential because incomplete thermal condensation leaves residual hydrogen-containing groups, such as NH or NH_2, which act as unwanted recombination centers for photogenerated electrons and holes, thereby reducing the overall hydrogen evolution rate [19, 23].

2.2 Chemical vapor deposition (CVD)

Chemical vapor deposition (CVD) provides another method for synthesizing g-C_3N_4, offering precise control over the material's thickness and morphology. In CVD, volatile precursors such as cyanamide are introduced into a high-temperature reactor, where they decompose and subsequently deposit as g-C_3N_4 onto substrates, as depicted in **Figure 4**. This technique enables the growth of thin films and nanostructures, making it suitable for photovoltaics and optoelectronics. However, CVD typically requires more specialized equipment and is associated with higher production costs [26-29].

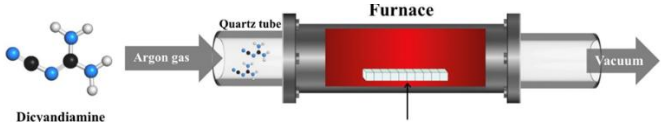

Figure 4. Schematic representation of the Chemical Vapor Deposition (CVD) system configuration for growing thin films and tailored nanostructures of g-C_3N_4 on solid substrates using volatile precursors.

This vapor-phase technique is highly suitable for integrated optoelectronic and photoelectrochemical devices because it offers strong control over the structural thickness and morphology of the catalyst at the atomic scale, as shown in the CVD arrangement (**Figure 4**). However, the requirement for specialized high-temperature reactors and vacuum infrastructure increases production costs and limits rapid large-scale commercial throughput compared with simple bulk thermal condensation [26-29].

2.3 Solvothermal and hydrothermal methods

Solvothermal and hydrothermal routes involve the reaction of precursors in high-pressure, high-temperature aqueous or organic solvents, as shown in **Figure 5**. These techniques offer the advantage of controlling the morphology and structure of g-C_3N_4 by adjusting the reaction conditions. The choice of solvent plays a critical role in determining the final properties of the material. Hydrothermal synthesis, in particular, is highly effective in generating hierarchical g-C_3N_4 structures that exhibit enhanced photocatalytic activity. These methods are advantageous for tailoring g-C_3N_4 to specific applications and have gained increasing attention in recent years [30-34].

Figure 5. An experimental schematic of the hydrothermal/solvothermal processing system used in high-pressure autoclave settings to construct hierarchical porous g-C_3N_4 structures.

Conducting the condensation process within closed chemical autoclaves enables precise control over structural nucleation and growth, as shown in the hydrothermal setup (**Figure 5**). The vapor pressure generated under high-temperature conditions guides the development of highly crystalline networks with enriched porosity. As a result, this liquid-phase modification outperforms traditional open bulk arrangements by increasing the total specific surface area and multiplying the active sites required for efficient fuel production [30-34].

2.4 Template-assisted synthesis

Template-assisted synthesis involves the use of templates, such as mesoporous silica or carbonaceous materials, to direct the formation of g-C_3N_4 with specific structural characteristics, as shown in **Figure 6**. By selecting templates with tailored pore sizes and shapes, researchers can control the surface area and porosity of g-C_3N_4, which are crucial factors influencing its photocatalytic performance. This method allows for the creation of g-C_3N_4 materials with finely tuned properties, making them suitable for applications such as pollutant removal and solar energy conversion [35-39].

3. g-C_3N_4 properties:

3.1 Thermal Behavior and Phase Transformation of g-C_3N_4

Yan et al. systematically investigated how melamine undergoes phase transitions when subjected to heating from ambient temperature to 1000 °C with a ramping rate of 10 °C per minute. As illustrated in **Figure 7a**, melamine undergoes sublimation and thermal condensation between 297 °C and 390 °C, indicated by a pronounced endothermic peak in the differential scanning calorimetry (DSC) analysis and a significant weight loss observed in the thermogravimetric analysis (TGA). Additional endothermic peaks at 545 °C and 630 °C are attributed to deamination and decomposition of the material, respectively [19].

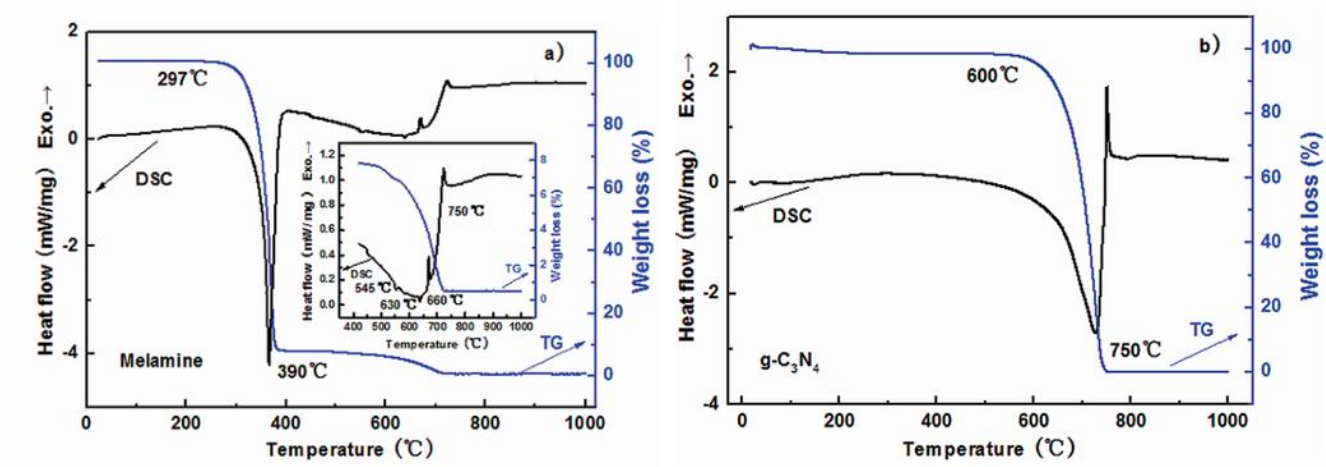

Figure 7. Thermal analysis profiles showcasing phase transformations and degradation boundaries of carbon nitride products: (a) Melamine thermal condensation pathways, (b) Chemical stability boundaries of extended g-C_3N_4 networks in open systems. Sub-figures (a,b) are reproduced with permission from Ref [19].

Figure 7b illustrates the thermal stability and phase transitions of g-C_3N_4 in an open atmosphere. The material exhibits notable stability below 600 °C, which is approximately 30 °C lower than the decomposition temperature of melamine (630 °C). Beyond this point, g-C_3N_4 undergoes decomposition into smaller molecular species such as CO_2 and NH_3. The thermal stability of g-C_3N_4 is significantly enhanced in a semi-closed ammonia atmosphere compared to an open system, primarily due to the suppression of deamination processes. Thermogravimetric analysis (TGA) results confirm that no residue remains at 750 °C [19].

The annealing temperature plays a crucial role in determining the structural properties of the final g-C_3N_4 material. Praus et al. employed melamine as a precursor for synthesizing g-C_3N_4 under an air atmosphere [40]. TGA analysis indicates that heating melamine to 400 °C leads to the formation of melen, primarily due to the release of ammonium groups. Upon further heating to 600 °C, melon is produced through the polymerization of melem [41]. At elevated temperatures, phases such as g-$C_6N_9H_2$ or g-$C_3N_{4.5}H$ exhibit greater stability compared to g-C_3N_4.

Moreover, the C/N molar ratio is strongly dependent on the thermal treatment temperature. The deviation of the C/N ratio from the theoretical value of 0.75 for g-C_3N_4 is primarily due to incomplete condensation of amino groups in melon and a relatively low degree of polymerization. Additionally, the reaction atmosphere significantly influences the structural characteristics of g-C_3N_4 by introducing defects and promoting

structural disorder. For example, thermal condensation of dicyanamide in a hydrogen atmosphere leads to increased nitrogen vacancy formation [42].

Operating near these thermal boundaries is highly critical for morphological engineering, as subtle temperature deviations directly disrupt the ideal C/N molar ratios. If the localized annealing temperature is too low, incomplete polymerization preserves unwanted hydrogen defects that trap charge carriers, whereas exceeding the thermal ceiling triggers severe decomposition of the heptazine network, dramatically reducing the overall mass yield [19, 40-42].

3.2 Band structure and optical activity

Both the electronic structures and optical responses of pure, B-modified, Zn-modified, and co-doped B-Zn tri-s-triazine g-C_3N_4 were investigated using first-principles methods. The results reveal that the band gaps of all doped g-C_3N_4 systems are reduced compared to that of pure g-C_3N_4. Specifically, the band gap of B-doped g-C_3N_4 is the smallest at 1.546 eV, while the band gaps of Zn-doped and B-Zn co-doped g-C_3N_4 are very close, measuring 2.047 eV and 2.100 eV, respectively. Despite the blue shift in the absorption peaks of all doped g-C_3N_4 systems, the absorption peak strength of B-Zn co-doped g-C_3N_4 decreases relative to that of pure g-C_3N_4. However, the optical absorption of the doped g-C_3N_4 materials is enhanced in the visible light range. For wavelengths greater than 405 nm but less than 526 nm, the optical absorption of B-Zn co-doped g-C_3N_4 is enhanced. Additionally, when the wavelength exceeds 526 nm, the optical absorption of all doped g-C_3N_4 systems is improved. Between 539 nm and 750 nm, B-Zn co-doped g-C_3N_4 exhibits the strongest optical absorption, followed by B- and Zn-doped g-C_3N_4. For wavelengths exceeding 750 nm, B-doped g-C_3N_4 shows the strongest absorption, followed by B-Zn co-doped g-C_3N_4 and Zn-doped g-C_3N_4 [43].

Table 1 summarizes the band gap values and main advantages of the nanocomposites investigated.

Table 1: Band gap and advantages of nanocomposites.

Nanocomposite	Band Gap (eV)	Advantage	Reference
Pure g-C_3N_4	2.7	Baseline material for comparison	[4]
B-doped g-C_3N_4	1.546	Smallest bandgap; enhanced optical absorption, particularly in the visible-light range	[43]
Zn-doped g-C_3N_4	2.047	Moderate bandgap reduction; good absorption properties, especially in the visible light range	[43]
B-Zn co-doped g-C_3N_4	2.100	Strong optical absorption between 539 nm and 750 nm; improved absorption for wavelengths >526 nm	[43]

3.3 Surface reaction and active sites

At the molecular level, as illustrated in **Figure 8**, the highest occupied molecular orbital (HOMO) within the g-C_3N_4 framework is primarily composed of N_2 orbitals, while the lowest unoccupied molecular orbital (LUMO) involves contributions from N_2, N_3, C_1, and C_2 atomic orbitals [44]. Consequently, nitrogen atoms serve as both oxidation and reduction active sites, while carbon atoms predominantly function as reduction active sites during photocatalysis [45]. Nevertheless, because chemical bonding forms a delocalized π-conjugated structure [46], spatially separating the oxidation and reduction sites remains challenging, limiting the number of available active sites. To overcome this limitation, recent engineering strategies, such as single-atom anchoring and vacancy engineering discussed later in this review, intentionally break this molecular symmetry to promote charge separation [47, 48].

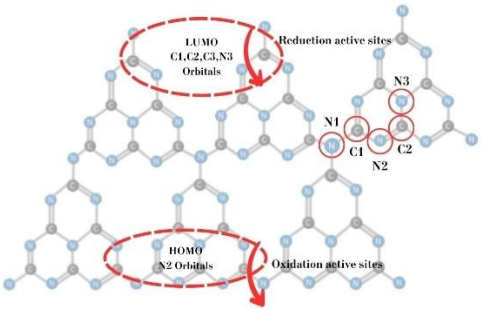

Figure 8. Spatial distribution and symmetry of localized frontier molecular orbitals (HOMO and LUMO) within the tri-s-triazine units of g-C_3N_4, mapping the specific atomic coordinates (C_1, C_2, N_1, N_2, N_3) that dictate photoredox reaction pathways and highlight the intrinsic spatial separation challenges *[made by biorender]*.

3.4 Mechanism of g-C_3N_4 Photocatalysis for Hydrogen Production

Hydrogen production via g-C_3N_4 photocatalysis has garnered significant attention as one of its most prominent application areas. According to the Gibbs free energy change for water splitting ($H_2O \rightarrow H_2 + ½O_2$, ΔG = 238 kJ/mol), the reaction requires sufficient energy input in accordance with thermodynamic principles [49]. Specifically, additional photon energy is needed to overcome the 1.23 eV energy barrier for effective water splitting. Therefore, g-C_3N_4 or its derivatives should possess an appropriate band gap, typically within the visible-light range, to efficiently harvest solar energy for photocatalytic water splitting [50].

However, the band-gap energy alone does not determine the photocatalytic performance. In addition to an appropriate band gap, the conduction band (CB) minimum must be more negative than the H^+/H_2 reduction potential, while the valence band (VB) maximum must be more positive than the H_2O/O_2 oxidation potential to enable the overall redox reactions. Furthermore, efficient charge separation, suppressed electron–hole recombination, rapid charge transport, and favorable surface reaction kinetics with low overpotentials are all critical factors governing hydrogen evolution efficiency [51, 52].

The separation of the valence band (VB) and conduction band (CB) is facilitated by the formation of a finite band energy gap [53]. Upon exposure to incident light, photo-excited charge carriers are generated, where electrons are excited from the VB to the CB, leading to the separation of the electron-hole pair, which is crucial for redox reactions [54].

The photocatalytic process generally involves several key steps presented in **Figure 9**. It starts with photon absorption, followed by the generation of electron-hole pairs (excitons). Subsequently, these excitons dissociate into free charge carriers, which diffuse through the photocatalyst toward the surface. However, rapid electron-hole recombination reduces the availability of charge carriers and consequently decreases the photocatalytic efficiency. Therefore, efficient charge separation and carrier transport to the photocatalyst surface are essential for promoting the surface redox reactions, enhancing the apparent quantum yield, and improving the overall hydrogen evolution performance [55, 56].

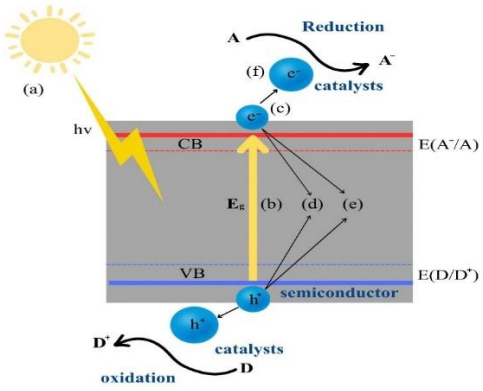

Figure 9. Comprehensive energy diagram and timeline of the multi-step photophysical cascade in semiconductor photocatalysis, illustrating the thermodynamic criteria for water splitting and the kinetic competition between useful surface redox pathways and unwanted charge carrier relaxation modes.

These stages form the basis for predicting appropriate modification strategies aimed at enhancing overall water splitting efficiency. Numerous studies have focused on the mechanism of photocatalysis. g-C_3N_4 exhibits high visible-light activity, attributed to its moderate bandgap. Because of the wide band gap and the overpotentials involved, the bandgap of g-C_3N_4 typically ranges from 2.0 eV to 3.1 eV, exceeding the minimum energy of 1.23 eV required for water splitting while remaining within the visible-light absorption range. The conduction band (CB) potential is sufficiently negative for H_2 production, positioning it favorably for hydrogen generation. Furthermore, the sp^2 hybridization in the 2D structure of g-C_3N_4 enables the formation of a layered architecture, facilitated by weak van der Waals forces between C and N atoms. The thermal conversion process promotes precursor condensation with a C/N molar ratio of approximately 0.75.

The photo-generated holes in g-C_3N_4 facilitate oxygen evolution from H_2O oxidation while preventing CO_2 mineralization through the generation of strong $OH^•$ radicals. However, low efficiency due to the high electron-hole recombination rate in smooth g-C_3N_4 has been observed, prompting significant research into enhancing active sites, introducing grain boundary defects, and optimizing charge carrier kinetics [55, 57]. Additionally, density functional theory (DFT)-based first principles have become widely adopted in photocatalysis research as an effective and rapid method for exploring ways to improve the photocatalytic performance of g-C_3N_4 [3, 52]. Leveraging semi-empirical

methods, such as Grimme, DFT-based approaches provide essential theoretical guidance for understanding and modifying the properties of g-C_3N_4, including lattice constants, density, cell volume, relative energy, electron structure, and absorption spectra [58].

3.5 Photocatalytic Hydrogen Production

It is important to distinguish between sacrificial hydrogen evolution (SHE) and overall photocatalytic water splitting (OWS) when evaluating the performance of g-C_3N_4-based photocatalysts. In many published studies, sacrificial agents such as methanol, ethanol, triethanolamine (TEOA), or lactic acid are intentionally added to consume photogenerated holes, thereby suppressing electron–hole recombination and significantly enhancing hydrogen evolution rates. While this approach is valuable for investigating the intrinsic hydrogen evolution reaction (HER) activity of photocatalysts, it does not represent true overall water splitting. In contrast, overall water splitting requires the simultaneous evolution of H_2 and O_2 from pure water without sacrificial reagents, which is considerably more challenging because of the sluggish oxygen evolution reaction (OER), higher kinetic overpotentials, and stricter charge separation requirements. Therefore, the hydrogen evolution rates reported under sacrificial conditions should not be directly considered as indicators of practical solar hydrogen production.

Accordingly, when comparing the photocatalytic performance of g-C_3N_4-based materials, careful consideration should be given to the reaction conditions, particularly whether hydrogen evolution was evaluated under sacrificial conditions or through overall water splitting [51, 59, 60].

4. Morphological Classifications and Structural Types of g-C_3N_4

The localized specific surface area, light-harvesting capacity, and spatial separation coordinates of photogenerated charge carriers of graphitic carbon nitride (g-C_3N_4) are all determined by its dimensionality and architectural geometry. Targeted morphological engineering enables the classification of g-C_3N_4 into discrete low-dimensional and hierarchical frameworks, each of which introduces specific physical benefits for visible-light-driven hydrogen evolution, departing from standard bulk configurations.

4.1 One-Dimensional (1D) Tubular Structures

One-dimensional (1D) architectures, such as nanotubes, nanorods, and nanowires, present a highly effective structural blueprint for accelerating directional charge migration. By confining electron transport along a single defined axial pathway, 1D tubular configurations drastically shorten the lateral diffusion distance that photogenerated carriers must travel to reach the catalyst-electrolyte interface. For instance, thin-walled g-C_3N_4 nanotubes fabricated via vapor-assisted surface reconstruction demonstrate remarkable performance gains. The hollow interior and minimized wall thickness facilitate rapid mass transport of reactants, reduce internal light-scattering losses, and limit the volumetric recombination of electron-hole pairs, thereby expanding the available catalytically active sites on both internal and external surfaces [47].

4.2 Two-Dimensional (2D) Nanosheets

Two-dimensional (2D) configurations, particularly ultrathin nanosheets, represent one of the most prominent structural classes for boosting photocatalytic efficiency. Atomically thin 2D layers completely overcome the severe mass-transport limitations and low surface areas inherent to dense bulk materials. The strategic exfoliation or direct synthesis of 2D g-C_3N_4 nanosheets results in an exceptional specific surface area, providing an abundance of exposed catalytic active sites for water adsorption. From an electronic standpoint, the structural thinning down to the nanoscale induces a quantum confinement effect, which shifts the band gap positions favorably, thereby increasing the thermodynamic driving force for the water reduction reaction. Furthermore, the migration pathway for photogenerated electrons from the bulk to the surface is reduced to a few atomic layers, suppressing recombination rates and ensuring rapid charge injection into co-catalysts [61-63].

4.3 Three-Dimensional (3D) Porous and Hierarchical Frameworks

Three-dimensional (3D) hierarchical frameworks and

interconnected porous networks integrate the benefits of low-dimensional building blocks into a stable, macroscopic structure. These complex architectures, such as macro/mesoporous flower-like structures or nanocorals, are often engineered using sacrificial template approaches or controlled hydrothermal assemblies. The primary advantage of 3D porous networks is their superior light-harvesting capability; the interconnected porous channels act as optical traps, inducing multiple internal light reflections and scattering events that maximize photon absorption efficiency. Additionally, the continuous 3D pathways provide an omnidirectional network for charge transport, while the highly porous matrix ensures rapid diffusion of electrolyte ions and immediate release of evolved hydrogen.

This prevents surface blocking by gas bubbles and helps maintain long-term catalytic stability [64, 65].

5. Recent Advances in g-C_3N_4-based Hydrogen Production Systems

Figure 10 presents a concise summary of recent progress in g-C_3N_4-based topologies for solar-driven hydrogen production, outlining the principal modification strategies addressed in this discussion.

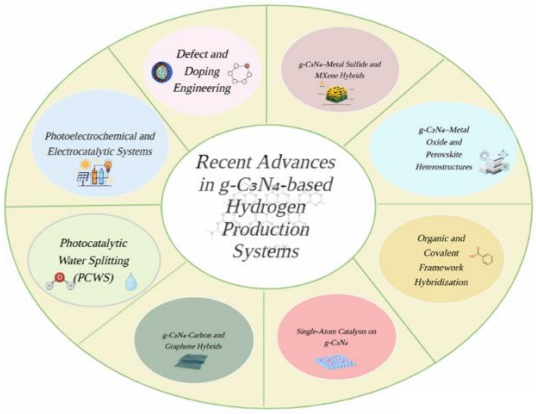

Figure 10. Recent Advances in g-C_3N_4-based Hydrogen Production System [made by biorender].

5.1 g-C_3N_4 in Photoelectrochemical and Electrocatalytic Systems

Through rational design strategies, incorporating graphitic carbon nitride (g-C_3N_4) into electrocatalytic devices has been shown to significantly improve catalytic performance. For example, using g-C_3N_4 nanosheets as supports for Co_3O_4 nanoparticles increased the active surface area and improved the oxygen evolution reaction (OER), lowering the overpotential to 375 mV and the Tafel slope to 123 mV dec^{-1} compared with pure Co_3O_4 [61]. Similarly, a $SmAlS_3$/g-C_3N_4 nanocomposite prepared by hydrothermal methods exhibited enhanced electrocatalytic activity for OER and hydrogen evolution reaction (HER), with low overpotentials of 278 mV and 305 mV, respectively, due to synergistic electronic interactions [66].

Conversely, photoelectrochemical (PEC) systems efficiently separate H_2 and O_2, suppress backward reactions, and generate relatively pure H_2. Photoelectrochemical water splitting is a promising technique for producing hydrogen energy. PEC systems offer several advantages over conventional photocatalytic and electrolytic water splitting, including low bias voltage, operational simplicity, minimal energy consumption, and high efficiency. Furthermore, the half-reactions that produce hydrogen and oxygen can occur at the photocathode and photoanode, respectively, making it easier to separate and collect these products [67]. A promising method for overcoming these fundamental limitations and achieving high-performance PEC water splitting is to construct g-C_3N_4-based nanosized heteroarrays as photoelectrodes, because they accelerate exciton separation and reduce the recombination of photogenerated electrons and holes [62].

The synergistic potential of photoelectrochemical water splitting using bifunctional Co_3O_4/g-C_3N_4 heterostructures was investigated. This method eliminated the requirement for external voltage from batteries by combining solar panel and electrochemical cell technologies. X-ray diffraction and scanning electron microscopy were used to verify the crystal structure and surface morphology of the produced Co_3O_4, Co_3O_4/g-C_3N_4, and Co_3O_4/Cg-C_3N_4 nanocomposites. The integration of carbon into the g-C_3N_4 framework markedly improved both catalytic activity and charge transport properties during visible-light-induced hydrogen and oxygen evolution. UV-visible spectroscopy revealed that Co_3O_4/Cg-C_3N_4 had a maximum absorption edge at 650 nm, corresponding to a band gap of 1.31 eV and increased light absorption. Among the three fabricated electrodes, Co_3O_4/Cg-C_3N_4 displayed the lowest Tafel slope of 112 mV/dec and a substantially lower overpotential of 30 mV. This increased photoelectrochemical efficiency was attributed to the well-established Z-scheme heterojunction between Co_3O_4 and g-C_3N_4. By extending the visible-light absorption range, this heterojunction improved charge separation. According to chronoamperometric analysis, the steady current maintained by the solar cell at a constant potential facilitated the efficient

application of Co_3O_4/g-C_3N_4 heterostructures for photo-assisted water splitting [68].

Recent research on adding graphitic carbon nitride (g-C_3N_4) to photoelectrochemical (PEC) and electrocatalytic systems is compiled in **Table 2** below, with an emphasis on design approaches and how they affect the evolution of hydrogen and oxygen.

Table 2: g-C_3N_4 in PEC and electrocatalytic systems.

System Composite	Design Strategy	Application Type	Performance Benefit	Ref.
g-C_3N_4 nanosheets + Co_3O_4 nanoparticles	Nanosheet support to increase active surface area	OER electrocatalysis	Lower overpotential (375 mV), Tafel slope 123 mV dec^{-1}	[61]
$SmAlS_3$/g-C_3N_4 nanocomposite	Hydrothermal synthesis for synergistic electronic interactions	OER & HER electrocatalysis	Low overpotentials (278 mV, 305 mV)	[66]
Co_3O_4/g-C_3N_4 heterostructures	Bifunctional PEC electrodes, Z-scheme heterojunction	Solar-driven water splitting	Overpotential 30 mV, Tafel slope 112 mV dec^{-1}, enhanced visible-light absorption (650 nm)	[68]

5.2 g-C_3N_4 for Photocatalytic Water Splitting (PCWS)

Identifying semiconducting materials with high photocatalytic water-splitting efficiency remains a major challenge, even though photocatalytic water splitting (PCWS) is a direct and promising route for producing hydrogen (H_2). Using an in situ hydrothermal technique, researchers prepared a 2D/2D NiAl-LDH/g-C_3N_4 heterojunction nanocomposite and demonstrated its photocatalytic capability for H_2 evolution from water splitting under simulated light irradiation. The optimized NiAl-LDH/g-C_3N_4 nanocomposite achieved an H_2 evolution rate of 3170 µmol h^{-1} g^{-1}, the highest value reported for the NiAl-LDH family. The enhanced photocatalytic efficiency is attributed to the formation of the 2D/2D heterojunction, which promotes electron-hole separation under light irradiation and improves electron conductivity [69]. Furthermore, another study reported that a recently developed composite electrocatalyst, (Fe, Cr)-ZnO/g-C_3N_4 ((Fe, Cr)-GZN), showed greater electrocatalytic performance. The composite material was produced by coprecipitating (Fe, Cr)-ZnO with g-C_3N_4, and its structure was thoroughly examined using key characterization methods. The catalysts were electrodeposited onto FTO glass for water-splitting studies. With a low OER overpotential of 304 mV and a Tafel slope of 89 mV dec^{-1}, the (Fe, Cr)-GZN composite showed strong electrochemical water-splitting ability, yielding a current density of 10 mA cm^{-2}. This performance demonstrates the potential of the (Fe, Cr)-GZN composite as an effective electrocatalyst for water splitting, outperforming both Cr-GZN and Fe-GZN composites [70]. In addition, another study showed that a two-dimensional $CuBiP_2Se_6$/g-C_3N_4 ferroelectric van der Waals heterojunction, with a suitable band gap of 1.78 eV, extended light absorption, and stronger redox ability than the two monolayer materials, is a capable candidate for photocatalytic water splitting. The ferroelectric polarization of the $CuBiP_2Se_6$ layer promotes the separation of photogenerated electron-hole pairs, greatly increasing charge-carrier lifetime. Gibbs free energy calculations further indicated that water photolysis can proceed spontaneously under visible-light irradiation. This study provides theoretical guidance for developing effective, stable, and reasonably priced photocatalysts in the future [71].

Furthermore, a simple hydrothermal process was used to prepare a g-C_3N_4/Ni_3S_2 composite for evaluating electrocatalytic OER performance in 1 M KOH electrolyte using physical and electrochemical characterizations. The nanocomposite exhibited large active regions with a high surface area. Its unique structure and morphology may promote charge transfer, contributing to improved durability over 30 hours. Electrochemical measurements further confirmed a reduced overpotential of 192 mV, a minimum Tafel slope of 35 mV dec^{-1}, and improved cyclic durability at an ideal current density of 10 mA cm^{-2}. The g-C_3N_4/Ni_3S_2 composite demonstrated remarkable electrocatalytic activity, showing a significantly lower Rct value of 2.7 Ω, an onset potential of 1.56 V, and an increased turnover frequency of 1.09 s^{-1}. These results indicate that adding g-C_3N_4 to a specific metal sulfide can enhance electrocatalyst performance and make it a viable candidate for future water-oxidation and OER applications [72].

With an emphasis on heterojunction design and photocatalytic hydrogen-generation ability, Table 3 summarizes recent studies on g-C_3N_4-based systems for PCWS.

Table 3: g-C_3N_4 in photocatalytic water splitting (PCWS).

System Composite	Design Strategy	Application Type	Performance Benefit	Ref.
NiAl-LDH/g-C_3N_4 2D/2D heterojunction	In situ hydrothermal formation	Photocatalytic H_2 production	H_2 evolution rate 3170 μmol h^{-1} g^{-1}, enhanced electron-hole separation	[69]
(Fe, Cr)-ZnO/g-C_3N_4 ((Fe, Cr)-GZN)	Coprecipitation, electrodeposition on FTO	Electrocatalytic water splitting	Low overpotentials (304 mV), Tafel slope 89 mV dec^{-1}, current density 10 mA cm^{-2}	[70]
$CuBiP_2Se_6$/g-C_3N_4 ferroelectric van der Waals heterojunction	Band gap engineering & ferroelectric polarization	Photocatalytic water splitting	Improved light absorption, enhanced electron-hole separation	[71]
g-C_3N_4/Ni_3S_2 composite	Simple hydrothermal, large active surface area	OER electrocatalysis	Overpotential 192 mV, Tafel 35 mV/dec, enhanced durability	[72]

5.3 - Defect and Doping Engineering

Latest reviews also highlight the design and synthesis of electrocatalytic O_2 and H_2 evolution reaction-based materials of g-C_3N_4, incorporating defect design, morphological modulation, and heterojunction organization for improving energy conversion and storage [73].

A recent study proposed a multi-step defect engineering approach to enhance the photocatalytic activity of g-C_3N_4. The researchers successfully created co-modified g-C_3N_4 containing both NHx vacancies and cyanamide defects (NCMCN) through secondary thermal condensation assisted by sodium. Experimental data and DFT simulations confirmed that these defect configurations decreased the band gap, expanded the specific surface area, and improved light absorption. As a result, NCMCN demonstrated noticeably enhanced photocatalytic activity, with a hydrogen evolution rate 10.65 times higher than that of bulk g-C_3N_4 (MCN) and superior to nitrogen-vacancy-modified NVMCN [64]. Among the many modification methods, sodium doping represents a facile yet efficient strategy for improving the photocatalytic performance of g-C_3N_4. Sodium has been shown to modulate its optical and electronic properties effectively. Hydrothermal polymerization of g-C_3N_4 in sodium hydroxide solution produced sodium-doped g-C_3N_4 with improved photocatalytic performance. Photoluminescence (PL) studies showed an inverse relationship between PL intensity and hydrogen generation rate, indicating that reduced radiative recombination corresponds to increased photocatalytic H_2 evolution. EDX, SEM, and XRD analyses confirmed the presence of g-C_3N_4, and these observations indicate that sodium doping successfully increases the photocatalytic activity of g-C_3N_4 [74].

In an earlier investigation, g-C_3N_4 thin-wall tubes with purposefully manufactured carbon flaws were created using a vapor-assisted surface reconstruction technique. This design suppressed both inner and exterior recombination of photoexcited carriers, improved mass transport, exposed a large number of active sites, and decreased wall thickness. Consequently, the improved g-C_3N_4 outperformed the majority of previously reported tubular structures and demonstrated a 25-fold increase in hydrogen production under visible light when compared to ordinary g-C_3N_4 [47].

Apart from its stability and adjustable electrical characteristics, graphitic carbon nitride (g-C_3N_4) is constrained by its wide band gap and insufficient charge separation. The effects of sulfur (S) and oxygen (O) interstitial doping on monolayer g-C_3N_4 were investigated using periodic density functional theory (DFT) simulations with VASP. The results showed that O and S doping widens the band gap and increases light absorption. However, single doping is insufficient to alter the band edge for effective photocatalytic hydrogen production. Co-doping with both O and S shifts the band edges, satisfying the energy-level requirements for hydrogen production. By localizing active sites at the band boundaries, the doped atoms improve electron-hole separation and provide theoretical insights for designing improved g-C_3N_4-based photocatalysts for efficient hydrogen production [75].

A three-dimensional P-doped flower-shaped macroporous g-C_3N_4 has been designed by researchers as a metal-free bifunctional photocatalyst for effective solar-to-chemical energy conversion. With hydrogen evolution of 4513.6 μmol h^{-1} g^{-1} and H_2O_2 production of 1321.3 μmol h^{-1} g^{-1},

respectively, the optimized 3DPCN10 (10 wt.%) showed noticeably improved performance. These values are around 4.3 and 7.2 times higher than those of pristine g-C_3N_4. Increased surface area, effective charge-carrier separation, and the interconnected P-doped porous framework were credited with this enhancement, which offered a novel technique to boost the photocatalytic activity of g-C_3N_4-based systems [65]. AgO nanoparticles and lanthanum-doped g-C_3N_4 nanosheets have been combined to create a novel Z-scheme photocatalyst (AgO/La@g-C_3N_4, ALCN). With improvements of 13-, 4-, and 2-fold over pristine g-C_3N_4, La-doped g-C_3N_4, and La-g-C_3N_4/Ag_2O, respectively, the composite demonstrated an exceptional hydrogen production rate of 16.7 mmol h^{-1} g^{-1} under solar irradiation. This exceptional activity and stability were ascribed to effective electron-hole separation made possible by Z-scheme charge transfer channels and La-induced energy states [63].

Structure-Activity Context on Doping and Defects:

From a fundamental standpoint, intrinsic electronic modulators like sulfur, phosphorus, or sodium doping narrow the structural bandgap or strategically shift the band edges to optimize energy levels required for visible-light capture [65, 74, 75]. Concurrently, defect engineering such as introducing carbon or nitrogen vacancies, or cyanamide functional groups creates intermediate sub-band electronic states within the forbidden band [64]. These induced states act as shallow trapping nodes that successfully prolong charge carrier lifetimes by preventing the immediate radiative recombination of photogenerated excitons [64, 74]. However, a critical chemical boundary exists: the localization of active sites at the boundaries must be precisely calibrated [75]. If the density of these dopants or structural defects exceeds an optimal threshold, the nodes transition into deep bulk recombination sinks that isolate charge carriers irreversibly, ultimately dropping the overall hydrogen evolution kinetics [64, 75].

Table 4 lists many doping and defect engineering techniques for g-C_3N_4 that enhance photocatalytic activity and hydrogen evolution performance.

Table 4: Defect and doping strategies in g-C_3N_4.

System Composite	Design Strategy	Application Type	Performance Benefit	Ref.
g-C_3N_4 with NHx vacancies & cyanamide defects (NCMCN)	Multi-step defect engineering	Photocatalytic H_2 evolution	10.65× higher H_2 evolution than bulk g-C_3N_4	[64]
Sodium-doped g-C_3N_4	Hydrothermal polymerization in NaOH	Photocatalytic H_2 evolution	Reduced radiative recombination, improved photocatalytic activity	[74]
g-C_3N_4 thin-wall tubes with carbon flaws	Vapor-assisted surface reconstruction	Photocatalytic H_2 evolution	25-fold H_2 production increase	[47]
O & S co-doped g-C_3N_4 monolayer	DFT-guided co-doping	Photocatalytic H_2 production	Band edge shift, improved electron-hole separation	[75]
P- doped 3D macroporous g-C_3N_4	Metal-free bifunctional photocatalyst	Solar-to-chemical conversion	H_2 evolution 4513.6 µmol h^{-1} g^{-1}	[65]
AgO/La@g-C_3N_4 Z-scheme photocatalyst	Z-scheme charge transfer & La-induced states	Photocatalytic H_2 evolution	16.7 mmol h^{-1} g^{-1}, 13× higher than pristine g-C_3N_4	[63]

5.4 Organic and Covalent Framework Hybridization

Researchers investigate the possibility of enhancing photocatalytic activity by modifying non-metallic molecules to customize the characteristics of two-dimensional graphitic carbon nitride (g-C_3N_4). In a recent study, g-C_3N_4-PMP, g-C_3N_4-BAB, and g-C_3N_4-HBAB nanosheet composites were created by thermally polymerizing melamine monomers with the help of organic materials, specifically (E)-2-((phenylimino)methyl) phenol, (E)-4-(benzylideneamino)benzoic acid, and (E)-4-((hydroxybenzylidene)amino)benzoic acid. The studied Schiff bases have a range of functions that can affect the porosity, surface reactive sites, and electronic structure. In comparison to pristine g-C_3N_4, all of the modified composites demonstrated

increased photocatalytic hydrogen production efficiency. Interestingly, g-C_3N_4-PMP exhibited the highest catalytic activity, with a rate of 1148 μmol h^{-1} g^{-1}, seven times higher than that of g-C_3N_4. To create a feasible process for photocatalysis, the optical and photoelectrochemical characteristics of the photocatalysts were examined. To synthesize g-C_3N_4, the incorporation of organic Schiff bases in combination with melamine offers a flexible way to customize the material's characteristics and enhance its photocatalytic performance for a range of energy and environmental applications [76]. For high-efficiency visible-light photocatalytic H_2 production, 2D/2D covalent organic framework/graphitic carbon nitride (COF/CN) van der Waals heterojunctions were easily created using an ultrasonic technique. The optimized COF/CN composites reached a maximum photocatalytic H_2 generation rate of 449.64 μmol h^{-1}, roughly five times that of pure CN (89.08 μmol h^{-1}). According to the characterization and experimental investigations, the synergistic impact of COF and CN helps to enhance photocatalytic hydrogen production by encouraging the interfacial migration and spatial separation of photoinduced e^--h^+ pairs. For photocatalytic energy conversion, this work might pave the way for the development and fabrication of efficient heterojunction-based photocatalysts [77].

The hybrid approaches that combine g-C_3N_4 with organic and covalent frameworks to improve photocatalytic hydrogen production are compiled in **Table 5**.

Structure-Activity Context on Framework Hybridization:

From a structural perspective, the incorporation of organic Schiff bases or 2D covalent organic frameworks (COFs) fundamentally alters the surface reactive configurations and electronic density distributions of the underlying g-C_3N_4 template. Pristine g-C_3N_4 typically suffers from low charge accessibility due to its high exciton binding energy. The introduction of tailored conjugated networks (such as PMP or COF matrices) sets up a non-covalent van der Waals 2D/2D interface that promotes an accelerated interfacial electronic vector. This structural hybridization effectively broadens the visible-light absorption spectrum and acts as an immediate charge-extraction cascade, isolating photoinduced electrons and holes across opposing structural skeletons. By optimizing internal porosity and mitigating the extreme spatial overlap of frontier molecular orbitals (HOMO/LUMO) over identical polymer networks, these hybrids drastically increase structural charge distribution efficiency while preserving strong redox driving potentials [76, 77].

Table 5: Organic and covalent framework hybrids with g-C_3N_4.

System Composite	Design Strategy	Application Type	Performance Benefit	Ref.
g-C_3N_4-PMP, g-C_3N_4-BAB, g-C_3N_4-HBAB	Schiff base thermal polymerization	Photocatalytic H_2 production	g-C_3N_4-PMP: 1148 μmol h^{-1} g^{-1}, 7× higher than pristine g-C_3N_4	[76]
COF/CN van der Waals heterojunction	Ultrasonic-assisted 2D/2D covalent hybridization	Visible-light photocatalytic H_2 generation	Up to 449.64 μmol h^{-1}, ~5× higher than pure CN	[77]

5.5 g-C_3N_4-Metal Oxide and Perovskite Heterostructures

The efficient conversion of solar energy into molecules by heterojunction photocatalysis has been extensively researched. However, obtaining effective electron transport between the components is the main obstacle in creating high-performing heterojunction photocatalytic devices. Here, g-C_3N_4 lamellae and $BaTi_2O_5$ nanorods were combined to create a unique S-scheme heterojunction photocatalyst. It has been demonstrated that the photocatalytic activity of g-C_3N_4 nanosheets with improved interfacial contact and strong electronic connection depends on the preferential deposition of Pt nanoparticles as cocatalyst using the one-step impregnation-reduction process. With great stability following cycles, the developed Ptimp/20$BaTi_2O_5$/g-C_3N_4 photocatalyst produces hydrogen at the ideal rate of 2587 μmol g^{-1} h^{-1}. According to theoretical calculations and photoelectrochemical investigation, the $BaTi_2O_5$/g-C_3N_4 heterojunction creation produces better charge carrier dynamics and staggered band alignment. This study emphasizes the significance and viability of using a novel S-scheme heterojunction with efficient cocatalysts to enhance photocatalysis [78].

Manganese vanadate ($Mn_2V_2O_7$) and graphitic carbon nitride (g-C_3N_4) composites were made for use in biosensing and electrocatalysis. The composites, which included 10 to 50% g-

C_3N_4, were created using a straightforward wet chemical process and subsequently assessed. According to a report, adding g-C_3N_4 increased $Mn_2V_2O_7$'s catalytic efficiency for the oxygen evolution reaction (OER) and the hydrogen evolution reaction (HER). The composite containing 30% g-C_3N_4 (CNMVO-30) performed the best. With better Tafel slopes and the lowest overpotentials for HER (466 mV) and OER (370 mV) in 0.1 M KOH, CNMVO-30 demonstrated quicker reaction kinetics. With improved stability, the composite obtained an overpotential of 479 mV at 10 mA cm^{-2} for total water splitting. Additionally, the study demonstrated that the composite demonstrated outstanding electrochemical sensing capabilities toward ascorbic acid (AA), providing steady performance across multiple cycles, good sensitivity, and a low detection limit (3.3 mM). According to these results, CNMVO-30 is a material that shows promise for energy conversion applications and biosensing platforms, offering a dual-functional catalyst that is both economical and effective [79].

Furthermore, in dopamine sensing, a RGO-g-C_3N_4-Co_3O_4 composite modified electrode possessed enhanced electrocatalytic activity with low detection limit of 8.10×10^{-7} M and excellent selectivity because of larger electroactive surface area and faster electron transfer [80]. Moreover, the combination of g-C_3N_4 with nonprecious-metal cocatalyst Ni_3N enhanced hydrogen evolution under visible light by increasing the hydrogen evolution rate by nearly three times while maintaining long-term stability [81].

Particularly, heterostructure formation like h-BN/flower-ring g-C_3N_4 with built-in electric fields offers a good potential to enhance charge transfer and photocatalytic efficiency [82]. In this regard, a recent work demonstrated La_2CrMnO_6/g-C_3N_4 Nanomaterials: Electronic interactions can be tuned by integrating perovskite oxides with g-C_3N_4. Strong interfacial coupling in La_2CrMnO_6/g-C_3N_4 composites leads to better visible light absorption and bandgap tuning. The development of an indirect bandgap, which encourages charge separation, is confirmed by electronic structure analysis. These nanocomposites are promising for next-generation energy conversion devices because they can be engineered for specific bandgap and charge transport properties, according to agreement between computational predictions and experiment [83]. Enhanced photocatalytic and electrocatalytic performance can be achieved by mixing g-C_3N_4 with metal oxides or perovskites, as shown in the accompanying **Table 6**.

Structure-Activity Context on Metal Oxide and Perovskite Heterostructures:

From a fundamental structure-activity perspective, coupling g-C_3N_4 with transition metal oxides or complex perovskite structures creates highly defined staggered band alignments (such as type-II, Z-scheme, or S-scheme heterojunctions) [78, 79, 83]. Pristine g-C_3N_4 exhibits rapid charge carrier recombination due to the severe spatial overlap of its native frontier molecular orbitals over identical polymer frames. The integration of secondary inorganic phases (e.g., $BaTi_2O_5$, $Mn_2V_2O_7$, or La_2CrMnO_6) introduces strong interfacial electronic interactions and built-in electric fields [78, 79, 83].

These generated junction potentials force an automated, unidirectional separation of photogenerated electrons and holes into opposing catalytic domains, effectively prolonging charge carrier lifetimes [78, 83]. Furthermore, when modified with specialized non-precious metal cocatalysts (such as Ni_3N or Pt clusters), the interface significantly reduces the kinetic overpotential barrier and accelerates interfacial electron transfer dynamics, preventing self-photocorrosion and dramatically boosting both hydrogen and oxygen evolution kinetics [78, 81].

Table 6: g-C_3N_4–metal oxide and perovskite heterostructures.

System Composite	Design Strategy	Application Type	Performance Benefit	Ref.
g-C_3N_4 + $BaTi_2O_5$ + Pt cocatalyst	**S-scheme heterojunction, one-step Pt impregnation**	**Photocatalytic H_2 production**	**2587 µmol g^{-1} h^{-1}, stable cycling**	**[78]**
$Mn_2V_2O_7$/g-C_3N_4 composites (10–50% g-C_3N_4)	**Wet chemical synthesis**	**OER & HER electrocatalysis**	**Optimal 30% g-C_3N_4: HER 466 mV, OER 370 mV overpotentials**	**[79]**
RGO-g-C_3N_4-Co_3O_4 composite	**Electrode modification**	**Dopamine sensing & H_2 evolution**	**Low detection limit 8.10 ×10^{-7} M, faster electron transfer**	**[80]**
g-C_3N_4 + Ni_3N	**Heterostructure formation**	**Visible-light H_2 evolution**	**~3× increased H_2 evolution**	**[81]**
h-BN/flower-ring g-C_3N_4	**Built-in electric field heterostructure**	**Photocatalytic H_2 production**	**Enhanced charge transfer & efficiency**	**[82]**
La_2CrMnO_6/g-C_3N_4	**Perovskite integration**	**Photocatalytic energy conversion**	**Tunable bandgap, better charge separation**	**[83]**

5.6 g-C_3N_4– Metal Sulfide and MXene Hybrids

For many years, metal-sulfide nanostructures have attracted scientific interest because of their distinctive optoelectronic characteristics. Several advanced applications, such as water splitting and hydrogen production, have benefited from substantial improvements in these materials. Research on semiconducting metal sulfides has also increased with the growing demand for low-dimensional materials, which require less material and often exhibit improved performance due to quantum-size effects. As a result, size-controllable nanostructures with diverse morphologies have been developed and investigated for potential applications [84].

Among metal sulfides, CdS is an intriguing option for a wide range of photocatalytic applications, including contaminant removal, organic compound conversion, and clean energy production. One study showed that CdS nanoparticles with essential functional groups were incorporated into g-C_3N_4 at loadings of 1%, 2%, and 3% to create CdS/g-C_3N_4 composites for improving hydrogen generation during $NaBH_4$ methanolysis. XRD and FTIR confirmed the successful incorporation of CdS, while TGA and SEM showed increased thermal stability and consistent CdS dispersion within the g-C_3N_4 matrix. UV-Vis analysis showed increased light absorption and a reduced band gap, and XPS confirmed strong electronic interactions that facilitated effective charge transfer and inhibited electron-hole recombination. The CdS 1%@g-C_3N_4 composite achieved the highest hydrogen evolution rate of 26,220 mL g^{-1} min^{-1} because of the optimal synergy and efficient electron transport between CdS and g-C_3N_4. However, increasing the CdS loading to 2% and 3% decreased the hydrogen evolution rates to 23,451 and 20,266 mL g^{-1} min^{-1}, respectively. This performance drop is systematically attributed to nanoparticle aggregation, which reduces the number of accessible catalytic active sites. The activation energies of the CdS@g-C_3N_4 nanocomposites increased with CdS concentration, from 30.32 kJ mol^{-1} for 1% CdS to 40.32 kJ mol^{-1} for 3% CdS, indicating a decline in catalytic efficiency. According to the Langmuir-Hinshelwood model, the methanolysis mechanism involves chemisorption of BH_4^- ions followed by hydrogen release. The synergistic effect of CdS and g-C_3N_4 greatly increases catalytic efficiency by improving BH_4^- adsorption and electron transport [85].

In contrast, MXene-based catalysts, which are two-dimensional transition-metal carbides and nitrides, have demonstrated significant potential in water-splitting applications because of their layered architecture, high conductivity, and adjustable surface terminations [86]. A study reported that combining g-C_3N_4 with MXene-based 2D materials has attracted considerable attention because of their improved conductivity, tunable surface chemistry, and large surface area. Recent advances in g-C_3N_4/MXene nanocomposites for enhanced photocatalytic H_2 production are highlighted in this research. In addition to their photocatalytic H_2 evolution, the structure, properties, and applications of type-II, Z-scheme, S-scheme, Schottky, and ternary heterojunctions are examined in detail. By facilitating efficient charge-carrier separation and electron transport, the combined effects of g-C_3N_4 and MXenes increase photocatalytic efficiency. Along with structure optimization and interface-engineering techniques, important challenges such as insufficient light absorption, charge-carrier mobility, long-term stability, and scalability are also discussed [87].

Building on this, a subsequent study investigated the use of innovative magnetic g-C_3N_4/MXene nanophotocatalysts for the photocatalytic destruction of pharmaceutical pollutants in wastewater. By adding Fe_3O_4, a novel compound with ferromagnetic characteristics was successfully formed, according to analyses. The g-C_3N_4/MXene magnetic catalyst demonstrated a superior decrease of 92% of clindamycin in actual wastewater after 120 minutes of exposure to sunshine. After two hours, a high organic carbon reduction of more than 38% was also noted. Expanding the interlayer spacing in g-C_3N_4 combined with MXene resulted in a larger surface area enriched with active sites, which in turn facilitated more efficient electron-hole transfer and enhanced the degradation performance. In addition, the catalyst retained stability across four consecutive cycles, consistently achieving a removal efficiency above 58%. These findings suggest that the material holds strong promise for practical applications in water purification [88]. Through a calcination process, TiO_2 produced from Ti_3C_2 MXene with varying thicknesses was used to create a range of g-C_3N_4/TiO_2 heterojunction photocatalysts. The successful production of type II heterojunctions, which allowed effective charge separation

and transfer, was validated by characterization. With hydrogen evolution rates of 8.26 and 11.6 mmol h^{-1} g^{-1}, respectively, the optimized composites CN/S-TO and CN/M-TO demonstrated improvements of 2.7 and 3.5 times over pristine g-C_3N_4. In addition to providing stable electron transport channels in comparison to the single-layer counterpart, multilayer-derived TiO_2 is credited with this improvement due to the close heterojunction interface, which encourages charge migration and inhibits recombination. These findings demonstrate the potential for designing effective g-C_3N_4-based photocatalysts for sustainable hydrogen production using MXene-derived TiO_2 with adjustable thickness [89].

Ubaid and co-workers (2025) examined how semiconductors and MXene-based nanocomposites could improve photocatalytic hydrogen evolution in the presence of visible light. By HF etching Ti_3AlC_2, they created $Ti_3C_2T_x$ MXene, which they then hydrothermally combined with g-C_3N_4 and CdS. XRD, SEM, TEM, UV-Vis DRS, PL spectroscopy, and XPS were used to evaluate the resultant composites, and gas chromatography under visible light irradiation was used to assess the amount of hydrogen produced. Based on the findings, MXene/g-C_3N_4 and MXene/CdS nanocomposites, when compared to their pristine counterparts, more than tripled their hydrogen evolution rates, achieving 3120 and 2850 μmol g^{-1} h^{-1}, respectively. Greater light absorption, more effective charge separation, and greater stability over several cycles were cited as the reasons for the improvement. The scientists came to the conclusion that MXene-based nanocomposites have a great deal of promise to advance the manufacturing of photocatalytic solar fuel [90].

Table 7 highlights g-C_3N_4 hybrids with metal sulfides and MXene materials for advanced photocatalytic hydrogen production and pollutant degradation.

Table 7: g-C_3N_4–metal sulfide and MXene hybrids.

System Composite	Design Strategy	Application Type	Performance Benefit	Ref.
CdS/g-C_3N_4 (1-3%)	**Nanoparticle incorporation**	**H_2 evolution via $NaBH_4$ methanolysis**	**Best 1% CdS: 26,220 mL g^{-1} min^{-1}, efficient electron transport**	**[85]**
g-C_3N_4/MXene 2D composites	**Layered heterostructure**	**Photocatalytic H_2 production**	**Enhanced conductivity, charge separation, surface area**	**[86, 87]**
g-C_3N_4/MXene + Fe_3O_4	**Magnetic photocatalyst**	**Pharmaceutical pollutant degradation**	**92% clindamycin removal, stable for 4 cycles**	**[88]**
g-C_3N_4/TiO_2 (MXene-derived)	**Calcination, type II heterojunction**	**Photocatalytic H_2 evolution**	**H_2 evolution 8.26–11.6 mmol h^{-1} g^{-1}, improved electron transport**	**[89]**
MXene/g-C_3N_4 & MXene/CdS	**HF-etched $Ti_3C_2T_x$ + hydrothermal**	**Visible-light H_2 evolution**	**3120 and 2850 μmol g^{-1} h^{-1}, 3× higher than pristine**	**[90]**

5.7 g-C_3N_4-Carbon and Graphene Hybrids

Numerous carbon compounds, including polymeric (g-C_3N_4), have seen a resurgence as promising alternatives in photocatalysis since their appealing metal-free characteristics, advantageous photoelectric qualities, and cost-effectiveness. The integration of both materials with optimal photocatalytic performance has been a central topic for numerous efforts in

recent years; nevertheless, the direct parameters for this new advancement have not yet been thoroughly compiled. For the creation of metal-free semiconductors in subsequent research, it is essential to completely comprehend the synergistic impacts of carbon and g-C_3N_4 materials on photocatalytic action [91].

In another study, one of Cu_3P/g-C_3N_4/3D-graphene composite exhibited superior bifunctional electrocatalysis for overall water splitting with minimized overpotentials and long-duration operational stability [92].

Advanced photocatalytic systems with improved charge carrier dynamics and broad-spectrum light absorption are required due to the growing environmental presence of pharmaceutical contaminants, particularly tetracycline antibiotics.

In order to enhance the photocatalytic degradation of tetracycline when exposed to visible light, a novel polyvinylpyrrolidone/graphene oxide-graphitic carbon nitride/nickel oxide (PVP/GO-g-C_3N_4/NiO, PGOGN10) nanocomposite material was created. Excellent constituent dispersion, good interfacial contact, and improved charge separation were all demonstrated by the nanocomposite PGOGN10. Furthermore, photoluminescence and diffuse reflectance spectroscopy analyses verified that the resulting ternary heterojunction had a longer absorption capacity for visible light and a significantly reduced charge recombination rate. An adequate surface area and close interfacial contact between the composite components were demonstrated by XRD, XPS, and HRTEM. The improved PGOGN10 composite outperformed pristine g-C_3N_4 (42%) and g-C_3N_4/NiO (67%), achieving 93.25 percent TC degradation after 90 minutes (rate constant: 0.045 min^{-1}) under the same experimental conditions. Superoxide radicals (•O_2-, 68.3%) and direct hole oxidation (24.1%) were found to play a major role in the photocatalytic degradation mechanism, according to radical scavenging experiments. This finding indicated the presence of a Z-scheme charge transfer mechanism, where GO functioned as an electron intermediary. Such an arrangement facilitated the spatial separation of the photogenerated charge carriers, while still maintaining the strong redox potentials of g-C_3N_4 (conduction band: −1.12 eV) and NiO (valence band: 2.34 eV). Additionally, the composite showed operational resilience across a broad pH range of 4-7 and strong photostability during four consecutive cycles (82.5 percent activity retention). The improved visible light absorption of g-C_3N_4, the easy charge transfer capabilities of GO, and the NiO surfaces enriched with holes work in concert to provide this stability and adaptability [93].

Table 8 gathers research on g-C_3N_4 when combined with carbon and graphene materials to enhance photocatalytic and electrocatalytic performance.

Table 8: g-C_3N_4–carbon and graphene hybrids.

System Composite	Design Strategy	Application Type	Performance Benefit	Ref.
Cu_3P/g-C_3N_4/3D-graphene	Composite fabrication	Bifunctional electrocatalysis	Minimized overpotentials, long-term stability	[92]
PVP/GO-g-C_3N_4/NiO (PGOGN10)	Ternary heterojunction	Photocatalytic degradation of tetracycline	93.25% TC degradation in 90 min, enhanced charge separation	[93]

5.8 Single-Atom Catalysts on g-C_3N_4

One novel approach for improving visible-light-driven H_2 generation by graphitic carbon nitride is the synergistic catalysis of metal single atoms and their nanoclusters; however, simultaneously anchoring metal single atoms and clusters remains challenging. To precisely control Au atom formation sites during the synthesis of Au quantum dots (QDs) on g-C_3N_4, a carbon vacancy trap technique was introduced. Under visible light, this photocatalyst (AuSA+QDs/CvCN) produced H_2 at a record rate of 1318.8 μmol h^{-1} g^{-1}. Characterization results showed that C vacancies and Au species work together to enhance visible-light utilization and optimize the energy band structure of CN. This greatly reduces the recombination of photogenerated carriers and improves charge separation and transport. DFT computations further confirmed that AuSA+QDs/CvCN optimizes carrier dynamics. The photocatalytic H_2 production efficiency is greatly increased through the synergistic effect of proton transport and electron transfer between Au single atoms and Au QDs,

along with the suppression of H_2 spillover. This work offers a valuable resource for designing and developing materials for high-efficiency photocatalytic H_2 production [48].

Researchers investigated the relationship between photocarrier behavior and the photocatalytic activity of g-C_3N_4 loaded with single Cu atoms for selective oxidation in water. The addition of single Cu atoms improves photoconductivity by increasing carrier mobility and extending the lifetime of photoexcited electrons, as demonstrated by transient microwave conductivity. This improvement increases the population of mobile electrons. Although pristine g-C_3N_4 does not exhibit detectable photoconductivity, it can still drive photocatalytic reactions, indicating that photoexcited electrons in g-C_3N_4 remain sufficiently reactive even when they are primarily trapped rather than recombined. The linear relationship between photocatalytic activity and the product of photoconductivity and electron lifetime demonstrates the value of this parameter as a descriptor for catalyst design. In performance tests, the photocatalysts produced benzaldehyde from benzyl alcohol under 455 nm irradiation with 100% selectivity, aromatic balance, and an apparent quantum yield of 0.82%, achieving a yield-to-power ratio of up to 1.1 mmol g^{-1} h^{-1} W^{-1}. The reaction proceeds under ambient conditions without additives or external oxidants. H_2O_2 is also generated at a rate of up to 0.26 mmol g^{-1} h^{-1} [94].

While single-atom Fenton-like catalysts anchored on graphitic carbon nitride (g-C_3N_4) exhibit strong promise for the removal of organic contaminants from water, their performance is often limited by structural irregularities and poor metal anchoring. To overcome these challenges, this study proposes a controlled synthesis strategy for developing iron single-atom catalysts (Fe-SACs) on a g-C_3N_4 /montmorillonite (MMT) heterostructure, ensuring a balance between metal precursor availability and the formation of effective anchoring sites. It was discovered that directional electron transfer from MMT to g-C_3N_4 improved interfacial electron redistribution, strengthened metal-support contacts, and markedly increased stability and catalytic activity. Over 2000 minutes of continuous flow operation, the optimized FNC-MMT (Fe@C_3N_4–MMT) SACs system exhibited >95% pollutant degrading efficiency. Its kinetic rate constant (k = 1.4404 min^{-1}) was 36-, 758-, and 2880-fold higher than that of Fe- C_3N_4 SACs, pristine g-C_3N_4, and individual MMT, respectively. The heterostructure demonstrated remarkable photocatalytic cycling ability under visible light, demonstrating the crucial function of interfacial electron synergy. As demonstrated by in situ electron spin resonance (ESR) and electrochemical analysis such as the galvanic oxidation process, mechanistic investigations showed that the system activates peroxymonosulfate (PMS) via a non-radical pathway dominated by $^1O_2$ production and direct electron transfer. Additionally, DFT studies showed that MMT lowers the energy barrier for PMS activation by optimizing the electronic structure of Fe sites. This work advances the design of high-efficiency water filtration systems by offering a scalable method for creating stable SACs and essential insights into electronic-structure-mediated non-radical catalysis [95].

Researchers used a highly diluted tetraamine palladium (II) chloride precursor to anchor Pd SAs onto graphitic carbon nitride (g-C_3N_4) using a technique known as "spontaneous deposition." With a relatively low Pd loading of 0.05 wt%, this method can produce a significant reduction in charge transfer resistance and maximize photocatalytic activity. In comparison to Pd nanoparticles deposited on g-C_3N_4 via conventional photodeposition, the resulting Pd SA-modified g-C_3N_4 exhibits an impressive hydrogen production efficiency of 0.24 mmol h^{-1} mg^{-1} Pd, which is more than 50 times higher. Pd SAs' ideal coordination within the g-C_3N_4 structure is responsible for the enhanced electron transport that results in this notable improvement in catalytic efficiency [96].

Moreover, single-atom Ir and Ru anchored on mesoporous graphitic carbon nitride (Ir-g-C_3N_4 and Ru-g-C_3N_4) have been synthesized for use as photocatalysts and electrocatalysts for the hydrogen evolution reaction (HER). Ru-g-C_3N_4 performs better than other advanced HER catalysts, Ir-g-C_3N_4, and the commercial Pt/C benchmark. The material demonstrates strong potential for practical use, delivering high apparent current density and mass activity in both acidic and alkaline media. Ru-g-C_3N_4 and Ir-g-C_3N_4 both exhibit exceptional catalytic stability, catalyzing HER continuously for 120 hours in both acidic and alkaline conditions [97].

Recent developments in single-atom catalyst (SAC) design on g-C_3N_4 are compiled in Table 9 below, with a focus on methods to improve selective oxidation, pollutant degradation, and visible light-driven hydrogen generation. Catalytic efficiency, charge separation, and electron transfer optimization are the main areas of emphasis.

Table 9: Single-atom catalysts on g-C_3N_4.

System Composite	Design Strategy	Application Type	Performance Benefit	Ref.
AuSA+QDs/ CvCN	Carbon vacancy trap for Au quantum dots	Photocatalytic H_2 generation	H_2 evolution 1318.8 µmol h^{-1} g^{-1}, enhanced charge separation	**[48]**
g-C_3N_4 + single Cu atoms	Single atom loading for selective oxidation	Photocatalytic selective oxidation & H_2O_2 generation	Increased photoconductivity, electron mobility, 0.26 mmol g^{-1} h^{-1} H_2O_2	**[94]**
Fe-SACs on g-C_3N_4/montmorillonite (FNC-MMT)	Controlled metal precursor and anchoring	Water pollutant degradation	>95% pollutant degradation over 2000 min, high stability & interfacial electron synergy	**[95]**
Pd SAs on g-C_3N_4	Spontaneous deposition, low Pd loading (0.05 wt%)	Photocatalytic H_2 production	0.24 mmol h^{-1} mg^{-1} Pd, >50× higher than Pd nanoparticles	**[96]**
Ir-g-C_3N_4 and Ru-g-C_3N_4	Single-atom anchoring on mesoporous g-C_3N_4	HER electrocatalysis	Ru-g-C_3N_4 shows high current density and mass activity, 120 h stability in acidic & alkaline media	**[97]**

5.9 Critical Comparative Analysis of Engineering Strategies

Table 10. Comprehensive comparative assessment of different modification strategies for g-C_3N_4 photocatalysts.

Modification Strategy	Hydrogen Evolution Rate (HER)	Charge Separation Efficiency	Visible-Light Absorption Edge	Operational Stability	Primary Bottleneck Addressed
Heteroatom Doping (B, S, P, Na) [65, 74, 75]	Moderate increase (4.3x to 10.6x over bulk)	Moderate; localizes active sites at band boundaries	High enhancement; narrows bandgap down to ~1.54 eV **[43]**	Moderate; potential thermal instability or dopant leaching	Broadening solar spectrum capture and intrinsic bandgap narrowing.
Defect Engineering (Vacancies) [58, 64]	High enhancement (up to 25-fold higher than pristine matrix)	High; defects act as shallow traps preventing immediate decay	Moderate expansion; introduces intermediate sub-band states	Moderate to Low; vacancies can accumulate irreversible oxidation	Overcoming high exciton binding energy and creating active trapping nodes.
Heterojunction Construction (Z/S-scheme, COFs) [68, 69, 77, 78]	Exceptional (3170 µmol h^{-1} g^{-1}) **[69]**	Maximum efficiency; drives carriers into opposing operational phases	High capability; couples g-C_3N_4 with narrow-band semiconductors	Maximum stability; prevents self-photocorrosion via spatial isolation	Mitigating severe spatial overlap of HOMO/LUMO over the same skeleton.
Cocatalyst Loading (Single-Atoms) [85, 94]	Record-breaking (up to 26,220 $mL \cdot g^{-1} \cdot min^{-1}$) **[85]**	Superior; acts as an immediate electron-sink to accelerate extraction	Insignificant shifts; mostly aids via localized plasmon resonance	High; single-atoms are strongly locked in vacancy traps	Lowering the excessive kinetic activation overpotential barrier.
Morphology Control (1D/2D/3D) [58, 65]	High geometric gains (188-fold enhancement through porous networks)	High; systematically decreases diffusion length to few atomic layers	Moderate; induces quantum confinement but multiplies scattering	Superior; high macro-porosity prevents gas bubble surface blocking	Overcoming low specific surface area and severe mass-transport constraints.

A systematic evaluation of the aforementioned modification strategies reveals that each approach targets a distinct physical bottleneck within the photocatalytic cycle of graphitic carbon nitride (g-C_3N_4). Heteroatom doping and defect engineering primarily function as *intrinsic electronic modulators*. Doping, particularly via non-metallic elements like

sulfur or phosphorus, successfully narrows the bandgap to maximize visible-light absorption spectrum capture; however, it often introduces deep bulk structural defects that can act as charge recombination centers if the local concentration is not precisely optimized. Similarly, while defect engineering (such as introducing carbon or nitrogen vacancies) yields exceptional increases in hydrogen evolution rates by providing localized active nodes, its long-term operational stability remains a critical concern due to the high risk of framework degradation under continuous chemical and solar exposure.

In contrast, heterojunction construction and cocatalyst loading operate as *extrinsic charge-extraction networks*. Creating multi-phase frameworks especially via advanced S-scheme or Z-scheme alignments with multi-dimensional materials like MXenes, graphene oxide, or covalent organic frameworks (COFs) [68, 77, 78, 87] provides the highest charge separation efficiency recorded in literature. These complex systems utilize built-in electric fields to spatially isolate reduction and oxidation pathways, thereby resolving the fundamental thermodynamic bottleneck caused by the extreme spatial overlap of HOMO and LUMO states over the identical heptazine units. Furthermore, this operational isolation effectively protects the underlying catalyst from photochemically induced corrosion, ensuring superior durability across extended cycling tests. When combined with single-atom cocatalysts (SACs) [94], the kinetic activation overpotential for water splitting is drastically lowered. While standalone cocatalysts do not significantly expand the native visible-light absorption window, their synergistic integration with vacancy traps delivers unprecedented, record-breaking hydrogen evolution metrics by accelerating the interfacial electronic transfer vector.

Finally, morphology control acts as the *geometric foundation* for all ongoing modification frameworks. Transitioning from dense bulk matrices to 1D tubes, ultrathin 2D nanosheets, or 3D hierarchical porous architectures does not fundamentally shift the structural band alignment. Instead, it systematically reduces the exciton migration distance from the bulk core to the active catalyst-electrolyte interface [58, 65], effectively suppressing spatial recombination rates while drastically expanding the specific surface area available for reactant adsorption.

Concluding Review Insight: The comparative metrics demonstrate that no single modification mode can simultaneously optimize all four photophysical parameters. Future research trajectories must move away from isolated strategy assessments and focus heavily on multi-strategic hybridization such as loading single-atom cocatalysts onto morphologically tailored, defect-engineered Z/S-scheme heterojunctions to achieve the rigid industrial targets required to transition g-C_3N_4 architectures from bench-scale systems to competitive green hydrogen production infrastructure.

6 Conclusion and Outlook

Graphitic carbon nitride (g-C_3N_4), with a well-defined bandgap of 2.7 eV and a configurable layered architecture, has unquestionably become a key metal-free organic semiconductor for solar-driven hydrogen synthesis. Defect engineering, heteroatom doping, and sophisticated heterojunction designs, such as Z/S-schemes, are examples of laboratory-scale advances that have significantly increased initial solar-to-hydrogen (STH) efficiency; however, a crucial bottleneck still exists. Because iterative material improvements have reached a saturation point in the field, a paradigm shift is urgently needed. Future studies must go beyond routine synthesis and address the following key operational gaps to transform g-C_3N_4 from a basic academic topic into an industrial reality:

Critical Research Gaps and Future Horizons

Long-Term Stability under Operational Realism: The majority of current literature reports catalyst longevity within idealized, short-term windows using pure water and sacrificial agents. Future efforts must rigorously evaluate g-C_3N_4 under realistic conditions, including natural water matrices containing competing ions, fluctuating organic pollutants, macro-scale pH variations, and intermittent natural solar light. Understanding the photo-corrosion mechanisms and chemical degradation of modified interfaces under these dynamic environments is paramount.

Scalable engineering and synthesis routes: Standard laboratory thermal polymerization often suffers from batch-to-batch variation, low yields, and inhomogeneous heat transfer. Developing robust pilot-scale synthesis protocols, such as continuous-flow reactors, automated spray-drying, or industrial-templated pyrolysis, is essential for producing high-

surface-area nanostructures with consistent morphology and catalytic reproducibility.

Catalyst Recovery and Recyclability: A major pragmatic hurdle for suspended powder
photocatalysts is their separation from the treated reaction mixture. Research must prioritize the
design of easily recoverable configurations, such as magnetic composite catalysts or the
immobilization of g-C_3N_4 onto structural, porous substrates (e.g., membranes, ceramic meshes, or monoliths) without compromising active site accessibility or light penetration.
Techno-economic analysis (TEA) and life-cycle assessment (LCA): To demonstrate industrial competitiveness against established grey-hydrogen technologies, comprehensive TEA models are needed to quantify the net cost per kilogram of H_2, energy payback times, and system capital expenditures (CAPEX). Concurrently, rigorous cradle-to-grave LCAs must validate the environmental credentials of g-C_3N_4, ensuring that precursor sourcing, solvent usage, and eventual catalyst disposal align with green chemistry principles.

System-Level Integration and Dual-Functionality: Maximizing the economic viability of g-C_3N_4
platforms involves moving away from isolated hydrogen evolution reactions. Future reactor designs should couple hydrogen production with high-value parallel processes, such as biomass valorization, selective organic transformations, or target pollutant degradation, to maximize overall solar energy utilization.

Declaration of generative AI and AI-assisted technologies in the writing process

During the preparation of this work, the author used ChatGPT/Quill to paraphrase the text. After using this tool/service, the author reviewed and edited the content as needed and takes full responsibility for the content of the publication.

Declaration of competing interest

The author declares that they have no known competing financial interests or personal relationships that could have appeared to influence the work reported in this review paper.

References

1. Chen, Y., et al., *Facile fabrication of three-dimensional interconnected nanoporous N-TiO2 for efficient photoelectrochemical water splitting.* Journal of materials science & technology, 2018. **34**(6): p. 955–960.
2. Wen, J., et al., *Photocatalysis fundamentals and surface modification of TiO2 nanomaterials.* Chinese Journal of Catalysis, 2015. **36**(12): p. 2049–2070.
3. Wen, J., et al., *A review on g-C3N4-based photocatalysts.* Applied surface science, 2017. **391**: p. 72–123.
4. Chen, M., et al., *Progress in preparation, identification and photocatalytic application of defective g-C3N4.* Coordination Chemistry Reviews, 2024. **510**: p. 215849.
5. Shiraishi, Y., et al., *Highly selective production of hydrogen peroxide on graphitic carbon nitride (g-C3N4) photocatalyst activated by visible light.* Acs Catalysis, 2014. **4**(3): p. 774–780.
6. Li, Y., et al., *Recent advances in g-C3N4-based heterojunction photocatalysts.* Journal of Materials Science & Technology, 2020. **56**: p. 1–17.
7. Liang, Q., et al., *Macroscopic 3D porous graphitic carbon nitride monolith for enhanced photocatalytic hydrogen evolution.* Advanced Materials (Deerfield Beach, Fla.), 2015. **27**(31): p. 4634–4639.
8. Ali, H., et al., *Recent advances, synthesis, modifications and photogenerated carrier dynamics of g-C3N4 for photocatalytic water splitting.* International Journal of Hydrogen Energy, 2025. **100**: p. 79–128.
9. Hosseini, S.E. and M.A. Wahid, *Hydrogen production from renewable and sustainable energy resources: Promising green energy carrier for clean development.* Renewable and Sustainable Energy Reviews, 2016. **57**: p. 850–866.
10. Ni, M., et al., *A review and recent developments in photocatalytic water-splitting using TiO2 for hydrogen production.* Renewable and Sustainable Energy Reviews, 2007. **11**(3): p. 401–425.
11. Noussan, M., et al., *The role of green and blue hydrogen in the energy transition—A technological and geopolitical perspective.* Sustainability, 2020. **13**(1): p. 298.
12. Zheng, Y., et al., *Graphitic carbon nitride polymers toward sustainable photoredox catalysis.* Angewandte Chemie International Edition, 2015. **54**(44): p. 12868–12884.
13. Wang, K., et al., *Sulfur-doped g-C3N4 with enhanced photocatalytic CO2-reduction performance.* Applied Catalysis B: Environmental, 2015. **176**: p. 44–52.
14. Sun, L.-J., et al., *Bimetallic ZnNi co-catalyst modified g-C3N4 nanosheets for highly efficient photocatalytic hydrogen evolution.* International Journal of

Hydrogen Energy, 2025. **98**: p. 1386–1395.
15. Zhao, H., et al., *A photochemical synthesis route to typical transition metal sulfides as highly efficient cocatalyst for hydrogen evolution: from the case of NiS/g-C3N4.* Applied Catalysis B: Environmental, 2018. **225**: p. 284–290.
16. Bhanderi, D., P. Lakhani, and C.K. Modi, *Graphitic carbon nitride (gC 3 N 4) as an emerging photocatalyst for sustainable environmental applications: A comprehensive review.* RSC Sustainability, 2024. **2**(2): p. 265–287.
17. Wang, Y., et al., *Facile one-pot synthesis of nanoporous carbon nitride solids by using soft templates.* ChemSusChem: Chemistry & Sustainability Energy & Materials, 2010. **3**(4): p. 435–439.
18. Ji, H., et al., *Photocatalytic degradation of 2, 4, 6-trichlorophenol over g-C3N4 under visible light irradiation.* Chemical Engineering Journal, 2013. **218**: p. 183–190.
19. Yan, S., Z. Li, and Z. Zou, *Photodegradation performance of g-C3N4 fabricated by directly heating melamine.* Langmuir, 2009. **25**(17): p. 10397–10401.
20. Zhang, Y., et al., *Porous graphitic carbon nitride synthesized via direct polymerization of urea for efficient sunlight-driven photocatalytic hydrogen production.* Nanoscale, 2012. **4**(17): p. 5300–5303.
21. Zhang, G., et al., *Polycondensation of thiourea into carbon nitride semiconductors as visible light photocatalysts.* Journal of Materials Chemistry, 2012. **22**(16): p. 8083–8091.
22. Dong, J., et al., *g-C3N4: properties, pore modifications, and photocatalytic applications.* Nanomaterials, 2021. **12**(1): p. 121.
23. Fang, H.-B., et al., *Facile large-scale synthesis of urea-derived porous graphitic carbon nitride with extraordinary visible-light spectrum photodegradation.* Industrial & Engineering Chemistry Research, 2016. **55**(16): p. 4506–4514.
24. Kharlamov, A., et al., *Features of the synthesis of carbon nitride oxide (g-C3N4) O at urea pyrolysis.* Diamond and Related Materials, 2016. **66**: p. 16–22.
25. Hayat, A., et al., *Graphitic carbon nitride (g–C3N4)–based semiconductor as a beneficial candidate in photocatalysis diversity.* International Journal of Hydrogen Energy, 2022. **47**(8): p. 5142–5191.
26. Yuan, B., et al., *Physical vapor deposition of graphitic carbon nitride (g-C3N4) films on biomass substrate: optoelectronic performance evaluation and life cycle assessment.* Advanced Composites and Hybrid Materials, 2022. **5**(2): p. 813–822.
27. Chebanenko, M., et al., *Chemical and structural changes of g-C3N4 through oxidative physical vapor deposition.* Applied Surface Science, 2022. **600**: p. 154079.
28. Chubenko, E.B., et al., *Chemical Vapor Deposition of 2D Crystallized g-C_3N_4 Layered Films.* 2022.
29. Yadav, R.M., et al., *Facile synthesis of highly fluorescent free-standing films comprising graphitic carbon nitride (gC 3 N 4) nanolayers.* New Journal of Chemistry, 2020. **44**(6): p. 2644–2651.
30. Raza, A., et al., *Hydrothermal synthesis of Fe3O4/TiO2/g-C3N4: advanced photocatalytic application.* Applied Surface Science, 2019. **488**: p. 887–895.
31. Kuldeep, A., R. Dhabbe, and K. Garadkar, *Development of g-C3N4-TiO2 visible active hybrid photocatalyst for the photodegradation of methyl orange.* Research on Chemical Intermediates, 2021. **47**(12): p. 5155–5174.
32. Idrees, F., et al., *In-situ synthesis of Nb2O5/g-C3N4 heterostructures as highly efficient photocatalysts for molecular H2 evolution under solar illumination.* Catalysts, 2019. **9**(2): p. 169.
33. Kunhikrishnan, L., K. Vishal, and S. Palaniyappan, *Mechanical and thermal characterization on synthesized silane-treated graphitic carbon nitride (g-C3N4) reinforced 3D printed poly (lactic acid) composite.* Journal of Inorganic and Organometallic Polymers and Materials, 2023. **33**(5): p. 1234–1245.
34. Wu, S., et al., *A simple synthesis route of sodium-doped g-C3N4 nanotubes with enhanced photocatalytic performance.* Journal of Photochemistry and Photobiology A: Chemistry, 2021. **406**: p. 112999.
35. Xi, J., et al., *Preparation of high porosity biochar materials by template method: a review.* Environmental Science and Pollution Research, 2020. **27**: p. 20675–20684.
36. Li, K., et al., *Template-assisted surface hydrophilicity of graphitic carbon nitride for enhanced photocatalytic H2 evolution.* ACS Applied Energy Materials, 2021. **4**(11): p. 12965–12973.
37. Li, F.-t., et al., *Precipitation synthesis of mesoporous photoactive Al2O3 for constructing g-C3N4-based heterojunctions with enhanced photocatalytic activity.* Industrial & Engineering Chemistry Research, 2014. **53**(50): p. 19540–19549.
38. Hao, M., et al., *In-situ hard template synthesis of mesoporous carbon/graphite carbon nitride (C/CN-Tx) composites with high photocatalytic activities under visible light irridation.* Solid State Sciences, 2020. **109**: p. 106428.
39. Liu, J., et al., *Controlled synthesis of ordered mesoporous g-C3N4 with a confined space effect on its photocatalytic activity.* Materials Science in Semiconductor Processing, 2016. **46**: p. 59–68.
40. Praus, P., et al., *Graphitic carbon nitride: Synthesis, characterization and photocatalytic decomposition of nitrous oxide.* Materials Chemistry and Physics,

2017. **193**: p. 438–446.
41. Giannakopoulou, T., et al., *Tailoring the energy band gap and edges' potentials of g-C3N4/TiO2 composite photocatalysts for NOx removal.* Chemical Engineering Journal, 2017. **310**: p. 571–580.
42. Tay, Q., et al., *Defect engineered g-C3N4 for efficient visible light photocatalytic hydrogen production.* Chemistry of Materials, 2015. **27**(14): p. 4930–4933.
43. Zhou, X., et al., *Influence of B, Zn, and B-Zn doping on electronic structure and optical properties of g-C3N4 photocatalyst: A first-principles study.* Results in Physics, 2021. **26**: p. 104338.
44. He, Q., et al., *Enhancement of photocatalytic and photoelectrocatalytic activity of Ag modified Mpg-C3N4 composites.* Applied Surface Science, 2017. **391**: p. 423–431.
45. Wang, X., et al., *A metal-free polymeric photocatalyst for hydrogen production from water under visible light.* Nature materials, 2009. **8**(1): p. 76–80.
46. Wang, X., S. Blechert, and M. Antonietti, *Polymeric graphitic carbon nitride for heterogeneous photocatalysis.* Acs Catalysis, 2012. **2**(8): p. 1596–1606.
47. Yang, B., et al., *Carbon defective g-C3N4 thin-wall tubes for drastic improvement of photocatalytic H2 production.* Carbon, 2023. **202**: p. 348–357.
48. Yang, D., et al., *Carbon Vacancies-Anchored AU Single Atoms and Quantum Dots Synergistically Enable Efficient Visible-Light-Driven H2 Production: Electronic State Optimization of G-C3n4.* Available at SSRN 5346009.
49. Takanabe, K., *Photocatalytic water splitting: quantitative approaches toward photocatalyst by design.* Acs Catalysis, 2017. **7**(11): p. 8006–8022.
50. Yuan, L., et al., *Photocatalytic water splitting for solar hydrogen generation: fundamentals and recent advancements.* International Reviews in Physical Chemistry, 2016. **35**(1): p. 1–36.
51. Hisatomi, T., J. Kubota, and K. Domen, *Recent advances in semiconductors for photocatalytic and photoelectrochemical water splitting.* Chemical Society Reviews, 2014. **43**(22): p. 7520–7535.
52. Ong, W.-J., et al., *Graphitic carbon nitride (g-C3N4)-based photocatalysts for artificial photosynthesis and environmental remediation: are we a step closer to achieving sustainability?* Chemical reviews, 2016. **116**(12): p. 7159–7329.
53. Malik, R. and V.K. Tomer, *State-of-the-art review of morphological advancements in graphitic carbon nitride (g-CN) for sustainable hydrogen production.* Renewable and Sustainable Energy Reviews, 2021. **135**: p. 110235.
54. Yang, Y., et al., *Progress in developing metal oxide nanomaterials for photoelectrochemical water splitting.* Advanced Energy Materials, 2017. **7**(19): p. 1700555.
55. Shoji, S., et al., *Photocatalytic uphill conversion of natural gas beyond the limitation of thermal reaction systems.* Nature Catalysis, 2020. **3**(2): p. 148–153.
56. Wang, Y., X. Wang, and M. Antonietti, *Polymeric graphitic carbon nitride as a heterogeneous organocatalyst: from photochemistry to multipurpose catalysis to sustainable chemistry.* Angewandte Chemie International Edition, 2012. **51**(1): p. 68–89.
57. Lin, B., et al., *Construction of novel three dimensionally ordered macroporous carbon nitride for highly efficient photocatalytic activity.* Applied Catalysis B: Environmental, 2016. **198**: p. 276–285.
58. Wei, B., et al., *Insight into the effect of boron doping on electronic structure, photocatalytic and adsorption performance of g-C3N4 by first-principles study.* Applied Surface Science, 2020. **511**: p. 145549.
59. Kudo, A. and Y. Miseki, *Heterogeneous photocatalyst materials for water splitting.* Chemical Society Reviews, 2009. **38**(1): p. 253–278.
60. Wang, Q. and K. Domen, *Particulate photocatalysts for light-driven water splitting: mechanisms, challenges, and design strategies.* Chemical Reviews, 2019. **120**(2): p. 919–985.
61. Li, X., et al., *Facile synthesis of Co_3O_4@ G-C_3N_4 nanocomposites as catalysts for oxygen evolution reaction in alkaline electrolyte.* Available at SSRN 4193501, 2022.
62. Wang, L., et al., *Graphitic carbon nitride (g-C3N4)-based nanosized heteroarrays: promising materials for photoelectrochemical water splitting.* Carbon Energy, 2020. **2**(2): p. 223–250.
63. Yaseen, H.S., et al., *La-Doped and AgO-Loading g-C3N4 Heterojunctions for Enhanced Photocatalytic Hydrogen Evolution from Water Splitting.* Materials Today Catalysis, 2025: p. 100111.
64. Guo, Y., et al., *Precise defect engineering g-C3N4 fabrication to improve hydrogen production performance.* Fuel, 2024. **362**: p. 130743.
65. Iqbal, W., et al., *Fabrication of interconnected flower-shaped macroporous P-doped g-C3N4 for enhancing visible-light-driven production of H2 and H2O2.* Materials Today Chemistry, 2024. **41**: p. 102315.
66. Iram, F., et al., *Fabrication and OER/HER electrochemical activity of Sm, Al assisted g-C3N4 nanocomposite for alkaline water splitting.* Journal of Alloys and Compounds, 2025. **1014**: p. 178603.
67. Zhuang, H., et al., *Construction of g-C3N4-based photoelectrodes towards photoelectrochemical water splitting: A review.* Journal of Alloys and Compounds, 2023. **969**: p. 172302.
68. Shabbir, S.A., et al., *Bifunctional Co3O4/g-C3N4 hetrostructures for photoelectrochemical water splitting.*

ACS omega, 2024. **9**(19): p. 21450–21458.
69. Sivagnanam, M., et al., *Enhancement of Photocatalytic H2 evolution from water splitting by construction of two dimensional gC3N4/NiAl layered double hydroxides.* Applied Surface Science, 2019. **509**: p. 144656.
70. Alhashmialameer, D., et al., *Improved catalytic performance of (Fe, Cr)-ZnO/g-C3N4 nanocomposite towards electrocatalytic water splitting for clean energy.* Solid State Sciences, 2025. **160**: p. 107823.
71. Li, J., et al., *A direct Z-scheme CuBiP2Se6/g-C3N4 heterojunction enhances the photocatalytic water splitting for hydrogen production: A DFT study.* Chemical Physics Letters, 2025. **869**: p. 142056.
72. Majeed, M., et al., *A g-CN/Ni3S2 hybrid nanostructures for water splitting: A step towards sustainable energy-storage applications.* Inorganic Chemistry Communications, 2025. **176**: p. 114242.
73. Hayat, A., et al., *Different dimensionalities, morphological advancements and engineering of g-C3N4-based nanomaterials for energy conversion and storage.* The Chemical Record, 2023. **23**(5): p. e202200171.
74. Kurita, Y., Aoki, M., & Ohtani, N. (2023). Fabrication of sodium-doped graphitic carbon nitride for photoelectrochemical water splitting into hydrogen. Japanese Journal of Applied Physics, 63(1), 01SP30. and I. 690.
75. Yuan, H., et al., *First-principles Investigations of Photocatalytic Performance of (O, S) Pore-doped g-C3N4 for hydrogen production.* Materials Today Communications, 2025: p. 113261.
76. Saleh, M.R., et al., *Modulating g-C3N4 photocatalyst for H2 production via water splitting: The impact of Schiff base incorporation.* Journal of Environmental Chemical Engineering, 2024. **12**(5): p. 113866.
77. Liu, Y., et al., *Covalent organic framework/g-C3N4 van der Waals heterojunction toward H2 production.* Inorganic Chemistry, 2023. **62**(7): p. 3271–3277.
78. Li, Y., et al., *One-step direct construction of S-scheme BaTi2O5/g-C3N4 heterojunction for enhanced photocatalytic hydrogen evolution.* Science China Materials, 2024. **67**(7): p. 2142–2152.
79. Sandali, Y. and F.K. Butt, *Synthesis of Mn-vanadate/g-C3N4 nanocomposites for electrocatalytic water splitting and ascorbic acid detection.* International Journal of Hydrogen Energy, 2025. **127**: p. 227–240.
80. Madhavan, A.S. and L. Rajith, *RGO-g-C3N4-Co3O4 Composite Modified Platinum Electrode for Electrochemical Detection of Dopamine.* Journal of The Electrochemical Society, 2024. **171**(11): p. 117507.
81. Ge, J., et al., *Integrating non-precious-metal cocatalyst Ni3N with g-C3N4 for enhanced photocatalytic H2 production in water under visible-light irradiation.* Chinese Journal of Catalysis, 2019. **40**(2): p. 160–167.
82. Sun, L., et al., *Multiple optimization strategies for improving photocatalytic performance of the h-BN/flower-ring g-C3N4 heterostructures: Morphology engineering and internal electric field effect.* Chemical Engineering Journal, 2022. **446**: p. 137027.
83. Azzu, R., Ahsun, A., & Elly, B. (2025). Computational Modeling of the Electronic Structure and Optical Properties of La2CrMnO6/g-C3N4 Nanocomposites: Correlating Theoretical Predictions with Experimental Data..
84. Mamiyev, Z. and N.O. Balayeva, *Metal sulfide photocatalysts for hydrogen generation: A review of recent advances.* Catalysts, 2022. **12**(11): p. 1316.
85. Alshammari, K., et al., *Synthesis and characterization of CdS@ g-C_3N_4 catalyst for enhanced hydrogen generation using methanolysis of sodium borohydride.* Journal of Alloys and Compounds, 2025. **1010**: p. 177590.
86. Raj, K., et al., *A comprehensive review on the MXene-based catalysts for hydrogen generation via water splitting processes.* Journal of Molecular Structure, 2025: p. 143534.
87. Mandari, K.K. and M. Kang, *g-C3N4/MXene-based heterostructures: advanced catalysts for efficient and sustainable renewable energy production.* Advances in Industrial and Engineering Chemistry, 2025. **1**(1): p. 14.
88. Abbas, H.A., K.K. Abbas, and A.M.A. Al-Ghaban, *Magnetic MXene/g-C3N4 nano catalyst for photocatalytic degradation of clindamycin contaminate in wastewater.* Results in Chemistry, 2025. **13**: p. 101934.
89. Shuaib, S.S.A., et al., *Ti3C2 MXene-Derived TiO2/g-C3N4 Heterojunctions for Highly Efficient Photocatalytic H2 Generation.* ChemCatChem, 2025. **17**(7): p. e202402152.
90. Ubaid, M.U.B., et al., *MXene-Based Nanocomposites for Enhanced Photocatalytic Hydrogen Production via Water Splitting.* Annual Methodological Archive Research Review, 2025. **3**(8): p. 594–606.
91. Cheng, L., et al., *Carbon–graphitic carbon nitride hybrids for heterogeneous photocatalysis.* Small, 2021. **17**(1): p. 2005231.
92. Riyajuddin, S., et al., *3D-graphene decorated with g-C3N4/Cu3P composite: a noble metal-free bifunctional electrocatalyst for overall water splitting.* ChemCatChem, 2020. **12**(5): p. 1394–1402.

93. Al-Wasidi, A.S., et al., *PVP-mediated graphene oxide integration in g-C3N4/NiO heterojunctions for enhanced photocatalytic tetracycline degradation.* Diamond and Related Materials, 2025. **158**: p. 112708.
94. Sudrajat, H., J. Phanthuwongpakdee, and J.C. Colmenares, *The role of single copper atoms in enhancing the photocatalytic activity of carbon nitride for selective oxidation.* Materials Chemistry Frontiers, 2025. **9**(12): p. 1917–1932.
95. Jin, C., et al., *Precise Synthesis of Fe Single-Atom Catalysts on Montmorillonite/g-C3N4 Heterostructures for Highly Efficient Fenton-like Degradation of Organic Pollutants.* Water Research, 2025: p. 124420.
96. Jeyalakshmi, V., et al., *Pd single atoms on gC 3 N 4 photocatalysts: minimum loading for maximum activity.* Chemical Science, 2025. **16**(11): p. 4788–4795.
97. Yu, Z., Li, Y., Torres-Pinto, A., LaGrow, A. P., Diaconescu, V. M., Simonelli, L., ... & Liu, L. (2022). Single-atom Ir and Ru anchored on graphitic carbon nitride for efficient and stable electrocatalytic/photocatalytic hydrogen evolution. Applied Catalysis B: Environmental, 310, 121318..